Nucleic Acids Research, 2026, **54**, gkag136
https://doi.org/10.1093/nar/gkag136
Molecular and Structural Biology

Structural basis of Cas8-independent Cas3 recruitment in Type I-F2 CRISPR–Cas

Thomas Noé Perry[1,†], Christopher-Nils Mais[2,†], Mariana Sanchez-Londono[3], Wieland Steinchen[2], Pauline A Plitzko[2], Lennart Randau[3], Patrick Pausch[4,*], C Axel Innis[1,*], Gert Bange[2,5,*]

[1]Univ. Bordeaux, Centre National de la Recherche Scientifique, Institut National de la Santé et de la Recherche Médicale, ARNA, UMR 5320, U1212, Institut Européen de Chimie et Biologie, Pessac F-33600, France
[2]Center for Synthetic Microbiology & Department of Chemistry, Philipps University Marburg, Marburg 35043, Germany
[3]Center for Synthetic Microbiology & Department of Biology, Philipps University Marburg, Marburg 35043, Germany
[4]LSC-EMBL Partnership Institute for Genome Editing Technologies, Life Sciences Center, Vilnius 10257, Lithuania,
[5]Max Planck Institute for Terrestrial Microbiology, Marburg 35043, Germany

*To whom correspondence should be addressed. Email: patrick.pausch@gmc.vu.lt
Correspondence may also be addressed to C. Axel Innis. Email: axel.innis@inserm.fr
Correspondence may also be addressed to Gert Bange. Email: gert.bange@synmikro.uni-marburg.de
†These authors contributed equally to this work.

Abstract

CRISPR–Cas systems provide adaptive immunity in prokaryotes by targeting and degrading invasive genetic elements. Among them, the Type I-F2 system represents the most compact Type I CRISPR–Cas variant, distinguished by the complete absence of both large (Cas8) and small (Cas11) subunits. In other Type I systems, Cas8 is essential for protospacer adjacent motif (PAM) recognition and for triggering Cas3 recruitment, while Cas11 stabilizes the Cascade backbone and guides the nontarget DNA strand during R-loop formation. To elucidate how I-F2 executes interference in their absence, we determined the cryo-electron microscopy structure of the I-F2 Cascade bound to target DNA and Cas3. Our structure reveals that Cas5 alone mediates PAM sensing, while Cas7 subunits directly recruit Cas3, which adopts a helicase-loaded conformation compatible with DNA engagement. We show how the helicase and C-terminal domains of Cas3 capture the displaced nontarget strand to initiate directional unwinding and degradation. These findings uncover key mechanistic adaptations that enable efficient interference without canonical large and small subunits and emphasize the mechanistic diversity among closely related Type I systems, including I-E, I-F1, and I-F2. These insights provide a structural basis for engineering the hypercompact I-F2 system for genome editing and biotechnological applications.

Graphical abstract

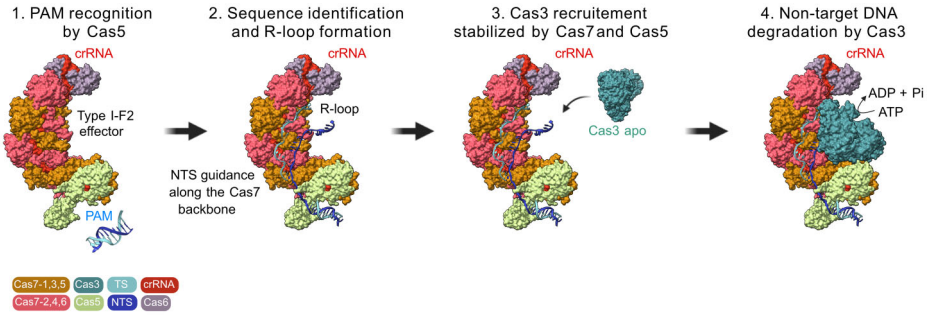

Introduction

CRISPR–Cas systems are RNA-guided adaptive immune systems found across the majority of archaea and bacteria, where they protect against invading mobile genetic elements (MGEs), such as bacteriophages, plasmids, and integrative conjugative elements [1–3]. These systems typically capture short foreign DNA fragments within clustered regularly interspaced palindromic repeat (CRISPR) arrays. Transcription and processing of these arrays generate small CRISPR RNAs (crRNAs) that guide Cas proteins to complementary nucleic acid targets, enabling sequence-specific degradation [4,5]. To avoid self-targeting, most DNA-targeting CRISPR–Cas sys-

Received: November 13, 2025. **Revised:** January 28, 2026. **Accepted:** February 2, 2026

tems require the presence of a short protospacer adjacent motif (PAM) flanking the target sequence, which is absent from the host CRISPR locus [6–8].

CRISPR–Cas systems are broadly categorized into two classes based on the composition of the interference complex. Class 1 systems (Types I, III, and IV) utilize multisubunit effector complexes, while Class 2 systems (Types II, V, and VI) rely on single, large, multidomain Cas proteins and are extensively used for genome engineering due to their simplicity [9–12]. Among Class 1 systems, Type I is the most widespread, comprising seven major subtypes (I-A through I-G) and several variants (e.g. I-F1, I-F2, I-F3, and I-F4) [9], distinguished by the architecture and composition of their signature interference complex known as Cascade (CRISPR-associated complex for antiviral defense) [9, 10, 13].

Recent structural studies have elucidated Cascade complexes across all known Type I subtypes [13–31, 32]. These assemblies share a conserved Cas7–crRNA backbone, but differ in their accessory subunits, such as Cas5, Cas6, and Cas8, which cap the backbone ends, and Cas11, which in some subtypes forms small subunits along the backbone. These variations define the subtype-specific architecture and mechanisms of Cascade. Structures capturing different mechanistic states, including PAM-bound seed bubbles and fully formed R-loops, have provided insights into target recognition and strand displacement during DNA surveillance [14, 15, 17, 18, 20, 22–25, 29, 31]. These conformational snapshots highlight subtype-specific mechanisms for DNA binding, crRNA-target strand (TS) pairing, and nontarget strand (NTS) displacement.

Effector recruitment strategies also diverge between subtypes. In Type I-E and I-F systems, PAM recognition and R-loop formation induce conformational activation of Cas8, allowing the recruitment of the helicase–nuclease Cas3 [33–38]. In contrast, Type I-F2 systems completely lack Cas8, and the mechanism by which Cas2-3f2 is recruited in its absence remains unclear. Additional complexity arises from the action of anti-CRISPR (Acr) proteins, which can inhibit Cascade by blocking PAM recognition, destabilizing R-loop formation, or preventing Cas3 recruitment, with Acr–Cascade structures described for Type I-C and I-F systems [17, 23, 26]. Recent review highlight the remarkable diversity of these Acr strategies targeting Type I systems, underscoring the evolutionary pressures shaping Cascade architecture [39]. In this context, the compact architecture of Type I-F2 may represent an adaptation to such selective pressures, although direct evidence for Acr-mediated targeting of I-F2 systems is currently lacking [11, 37, 40]). Despite these advances, complete ternary/quaternary structures of interference-competent complexes (Cascade bound to crRNA, and target DNA) with the Cas3 are currently available only for specific variants of subtypes I-A, I-C, and I-E [14, 18, 22] (see Table 1). Full effector assemblies for the other subtypes remain unresolved, leaving substantial gaps in our understanding of how interference is executed in these systems.

Among these, Type I-F2 (previously designated I-Fv) represents the most compact Type I variant, encoding only four Cas proteins (Cas6f2, Cas5f2, Cas7f2, and Cas2-3f2) and a minimal CRISPR array composed of 27 bp repeats and 32 bp spacers [24, 42, 43]. In Type I-F2 systems, the effector nuclease is encoded as a Cas2-Cas3 fusion protein (Cas2-3f2). Because our analyses focus on the helicase–nuclease activity of this protein, we refer to this module simply as Cas3 throughout the manuscript. Type I-F2 systems are commonly associated with MGEs such as plasmids and genomic islands [33, 44–46], and their compact architecture may reflect adaptation to size constraints or evasion of Acrs targeting related Type I-F1 systems [24]. DNA interference in Type I-F2 is initiated by recognition of a minimal 5′-GG-3′ PAM by Cas5, followed by crRNA-guided pairing of the TS along the Cas7 backbone. Concurrently, the NTS is displaced and guided along a conserved groove toward Cas6, forming a characteristic R-loop [5, 42]. Beyond their natural defensive role, compact Type I-F2 systems are emerging as promising genome editing tools due to their minimal protein requirements and high targeting specificity. Engineered variants have been successfully repurposed for targeted DNA degradation, transcriptional modulation, and genome engineering in both bacterial and eukaryotic contexts, leveraging their processive Cas3 nuclease activity for large-scale DNA removal or controlled editing [44–46]. Such systems offer potential advantages over Class 2 effectors, including expanded targeting range, reduced off-target effects, and the ability to perform long-range deletions, positioning Type I-F2 as an attractive platform for synthetic biology and therapeutic applications [47–49].

In contrast to I-E and I-F1 systems, where Cas3 recruitment is mediated by conformational changes in Cas8 [34–38], the absence of Cas8 in I-F2 raises questions about how the effector nuclease is engaged. Here, we show that Cas3 binds centrally within the I-F2 Cascade–R-loop complex, positioned between Cas5 and Cas6. Recruitment is stabilized by multivalent contacts with the Cas7 backbone together with extensive interactions with the displaced NTS, which together entangle Cas3 into the complex. Complementary hydrogen–deuterium exchange mass spectrometry (HDX-MS) revealed conformational changes within Cas3 upon recruitment, while Cascade subunits showed no additional protection beyond the R-loop state, consistent with Cas3 undergoing the major structural rearrangements required for interference. Our cryo-EM structure of the I-F2 Cascade–Cas3 complex reveals how the displaced NTS is threaded through the helicase core of Cas3 and delivered to the nuclease domain for processive DNA degradation. These findings illustrate a mechanistic divergence from Type I-E and I-F1 systems and establish a structural foundation for harnessing the hypercompact Type I-F2 system in genome editing applications.

Materials and methods

Plasmid construction

Recombinant expression of the Type I-F2 Cascade subunits Cas5f2, Cas6f2, and Cas7f2, together with crRNA, was performed using constructs described previously by Gleditzsch *et al.* [43] (plasmids *pCas1* and *pCRISPR-wt*). For production of Cas3, the *cas3* gene was cloned into a modified pET-24d expression vector containing BsaI restriction sites, thereby introducing an N-terminal His_6-tag for affinity purification.

To generate spacer variants for the efficiency of transformation (EoT) assay, the *crRNA-WT* plasmid was amplified by vector polymerase chain reaction (PCR) using primers *pUC19-AarI-fwd* and *pUC19-AarI-rev*, introducing AarI restriction sites. The resulting linearized plasmid was digested with AarI, and pairs of annealed oligonucleotides (*R1 fwd/R1 rev* and *R2 fwd/R2 rev*) were ligated into the vector, thereby

Table 1. Available structures of Type I Cascade effector complexes

Type	Organism	States	PDB	Citation
A	*Pyrococcus furiosus*	CascadeCascade–Cas3Seed bubble–Cas3R-loop–Cas3	7TR67TR87TR97TRA	[14]
B	*Synechocystis sp. PCC 6714*	Seed bubbleR-loop	8H678IPO	[15]
C	*Desulfovibrio vulgaris*	Cascade	7KHA	[16]
C	*Desulfovibrio vulgaris*	CascadeSeed bubbleR-loopCascade–AcrIF2 Cascade–AcrIC4	8DEX8DFA8DEJ8DFS8DFO	[17]
C	*Neisseria lactamica*	CascadeSeed bubbleR-loopR-loop–Cas3Cascade–AcrIC8Cascade–AcrIC9	8GAF8GAM8GAN8G9U8G9S8G9T	[18]
D	*Synechocystis sp. PCC6803*	Cascade (7.2 Å)	EMD-22 912	[19]
D	*Synechocystis sp.* PCC6803	CascadeR-loop	7SBB7SBA	[20]
E	*Escherichia coli*	Cascade	4U7U	[21]
E	*Thermobifida fusca*	Seed bubbleR-loop	5U075U0A	[41]
E	*Thermobifida fusca*	R-loop–Cas3	6C66	[22]
F	*Pseudomonas aeruginosa*	CascadeSeed-bubbleCascade–AcrF1Cascade–AcrF2Cascade–AcrF10	6B456B446B466B476B48	[23]
F	*Shewanella putrefaciens*	(Shortened) CascadeR-loop	5O7H5O6U	[24]
F	*Pseudomonas aeruginosa*	R-loop	6NE0	[25]
F	*Shewanella putrefaciens*	R-loop–Cas3	9G44	This study
F	*Selenomonas sp.* RGIG9219	Partial R-loopR-loopSingle stranded (ss) DNA-bound states	8Z0L8Z0K8ZNR	[32]
G	*Thioalkalivibrio sulfidiphilus*	Cascade	8ANE	[13]

creating BsaI sites. These BsaI sites were subsequently used to insert custom spacer sequences by ligation of annealed oligo pairs.

Complex purification and reconstitution

Genes encoding *S. putrefaciens* CN32 Cas5, Cas6, and Cas7 proteins were amplified by PCR and cloned into pRSFDuet-1 (Novagen), and *cas3* into pET24d (Novagen). Cas7 and Cas3 were fused to N-terminal His_6 tags. The Cascade proteins and the pre-crRNA substrate were coproduced in *E. coli* BL21(DE3) (Novagen) by incubating at 30°C overnight in LB-medium containing 1.25% (w/v) lactose. For the production of Cas3, *E. coli* BL21(DE3) pLysS (Novagen) were utilized. A culture in LB medium was incubated at 37°C until OD 0.6 was reached, when expression was induced by adding 1 mM Isopropyl-β-D-thiogalactopyranosid (IPTG) f.c., followed by 3 h of incubation at 20°C. Cells were lysed by a Microfluidizer (M110-L, Microfluidics). Cell debris after lysis was removed by high-speed centrifugation (41 000 rpm, rotor Beckman Coulter Ti45) at 4°C for 45 min. All proteins were purified by nickel-ion affinity (lysis and washing buffer: 20 mM HEPES-Na, pH 8, 250 mM NaCl, 20 mM KCl, 20 mM $MgCl_2$, and 20 mM imidazole; elution buffer: lysis buffer + 480 mM imidazole) and size-exclusion chromatography (SEC), as described previously [24]. The SEC buffer for Cascade consisted of 20 mM HEPES-Na (pH 7.5), 200 mM NaCl, 20 mM KCl, and 20 mM $MgCl_2$. For the SEC of Cas3, a buffer consisting of 20 mM HEPES-Na (pH 7.5), 500 mM NaCl, 20 mM KCl, 20 mM $MgCl_2$, and 2% (v/v) glycerol was used. TS and NTS were obtained from Sigma–Aldrich and combined in a 1:1.5 ratio (buffer: 20 mM HEPES-Na, pH 7.5, 50 mM NaCl) and heated to 95°C for 5 min, forming the R-loop precursor. The final complex was formed in two steps: first, 15 nmol of each, Cascade and R-loop precursor were incubated in 400 µl SEC buffer for 10 min at room temperature (RT). Second, 25 nmol of purified Cas3 were added prior to another 5 min of incubation at RT. The solution was then subjected to SEC on a Superdex 200 Increase 10/300 GL. The fractions containing protein were analyzed by sodium dodecyl sulfate–polyacrylamide gel electrophoresis (SDS–PAGE) and the fully assembled complex was used for further experiments.

Cryo-EM grid preparation

For cryo-EM analyses, 3 µl of 0.8 mg/ml purified Cascade/R-loop/Cas3 complexes were applied to a glow-discharged Quantifoil holey carbon grid (R2/2, 300 mesh). Grids were blotted with filter paper to remove excess sample for 4 s and plunge-frozen in liquid ethane using a Vitrobot Mark IV (Thermo Fisher Scientific) with a blotting force of 0 in an environment with the humidity and temperature set to 100% and 4°C, respectively.

Cryo-EM data acquisition

Cryo-EM movie data were collected in counting mode on a Talos Arctica (Thermo Fisher Scientific) operated at 200 kV and equipped with a K2 Summit direct electron detector (Gatan) in Nanoprobe mode at the IECB in Bordeaux (France). A magnification of 45 000× was applied to record 37 movie frames using SerialEM v4.0.9 [50], with an exposure time of 3.7 s using a dose rate of 1.35 electrons per $Å^2$ per frame for a total accumulated dose of 49.8 electrons per $Å^2$ at a pixel size of 0.93 Å. The final dataset was composed of 7698 micrographs with defocus values ranging from −0.4 to −1.6 µm (see Table 2).

Cryo-EM image processing

Data were processed in Relion v5.0 [51] according to the scheme presented in (Supplementary Fig. S1). Briefly, all frames were corrected for gain reference, motion-corrected and dose-weighted using MotionCor2 [52]. The resolution range of each micrograph and the contrast transfer function were estimated with CTFFind v4.1.14 [53]. Particles on micrographs were picked automatically in box sizes of 240 pixels and with an inter-box distance of 150 Å. Then, picked particles were classified into two-dimensional class averages to

Table 2. Data collection, processing, and refinement statistics of R-loop-Cas3-Cascade (PDB: 9G44)

Data collection and processing	
Magnification	45 000
Voltage (kV)	200
Electron exposure ($e^-/Å^2$)	49.773
Defocus range (μm)	−0.4 to −1.6
Pixel size (Å)	0.93
Symmetry imposed	C1
Initial particle images (no.)	2, 463, 680
Final particle images (no.)	1, 040, 370
Map resolution (Å)	3.2
FSC threshold	0.143
Map resolution range (Å)	3.0 to 5.0
Refinement	
Initial model used (PDB code)	5O6U
Model resolution (Å)	3.2
FSC threshold	0.143
Map sharpening B factor ($Å^2$)	−10
Model composition	
Chains	13
Non-hydrogen atoms	28 168
Protein residues	3190
Nucleotides	135
Ligands	2 (Mg^{2+})
B-factor (A^2)	
Protein	59.55
Nucleotide	77.77
Ligand	158.16
R.m.s deviations	
Bond lengths (Å)	0.004
Bond angles (°)	0.568
Validation	
Model-to-map CC	0.84
MolProbity score	1.20
Clashscore	2.69
Poor rotamers (%)	0.04
Cβ outliers (%)	0.00
Ramachandran plot	
Favored (%)	97.24
Allowed (%)	2.76
Disallowed (%)	0.00

identify homogeneous subsets using a regularization value of $T = 2$. The total number of initial extracted particles 2 463 680) was reduced to 1 040 370 by subsequent rounds of two-dimensional classifications. An initial model at 15 Å was generated and used as reference map for three-dimensional classification. This yielded a map at 5.1 Å, which was used as reference for high-resolution refinements in Relion v5.0's 3D auto-refinement. The resolution for the electron density map was estimated using the "gold standard" criterion (FSC = 0.143) resulting in a final reconstruction with an overall resolution of 3.2 Å. Local-resolution estimation was carried out using Relion v5.0. The volumes obtained were subjected to Auto-sharpening in the Phenix software package [54]. The pixel size was optimized by calculating model-to-map correlation coefficients at multiple pixel sizes in Chimera v.1.16 [55] and selecting the pixel size that yielded in the highest coefficient value.

Atomic model building and refinement

An initial model of the R-loop–Cas3 complex was obtained by placing the coordinates of the Cascade–I-Fv R-loop complex from *S. putrefaciens* (PDB 5O6U) [24] into an auto-sharpened map obtained with Phenix v.1.20.1 [56]. The crRNA, TS, NTS, and Cas3 protein were modelled *de novo* into the corresponding density using Coot v.0.9.7 [57]. The model was refined using Isolde v.1.3 [58] and the real space refinement procedure in Phenix v.1.20.1 [59], with reference model restraints (see Table 2).

Hydrogen–deuterium exchange mass spectrometry

Prior to HDX-MS, samples of Cascade, Cascade/DNA, Cascade/DNA/Cas3, or Cas3 were purified by SEC as described above. The preparation of HDX reactions was aided by a two-arm robotic autosampler (LEAP technologies) as described previously [60]. In brief, 7.5 μl of protein sample (concentration of ∼40 μM) were mixed with 67.5 μl of D_2O-containing SEC buffer (20 mM HEPES-Na, pH 7.5, 100 mM NaCl, 10 mM $MgCl_2$, 50 μM AMPPNP) to start the exchange reaction. After incubation for 10, 30, 95, 1000, or 10 000 s at 25°C, 55 μl of the reaction were withdrawn and mixed with 55 μl quench buffer (400 mM KH_2PO_4/H_3PO_4, 2 M guanidine-HCl, pH 2.2) temperated at 1°C. Ninety-five microliters of this quenched reaction were immediately injected into an ACQUITY UPLC M-Class System with HDX Technology (Waters) [61]. Non-deuterated samples were prepared in similar manner by 10-fold dilution into H_2O-containing SEC buffer. Injected sample was flushed out of the loop (volume of 50 μl) with H_2O + 0.1% (v/v) formic acid at a flow rate 100 μl/min flow rate, guided to a protease column (2 mm × 2 cm, immobilized porcine pepsin) kept at 12°C and the peptic peptides thus generated were collected on a trap column [2 mm × 2 cm, POROS 20 R2 (Thermo Fisher Scientific)] kept at 0.5°C. After 3 min, the trap column was placed in line with an ACQUITY UPLC BEH C18 1.7 μm 1.0 × 100 mm column (Waters), and peptides were eluted at 0.5°C using a gradient of H_2O + 0.1% (v/v) formic acid (A) and acetonitrile + 0.1% (v/v) formic acid (B) at a flow rate of 30 μl/min using the following program: 0–7 min/95%–65% A, 7–8 min/65%–15% A, 8–10 min/15% A, 10–11 min/5% A, 11–16 min/95% A. Eluting peptides were guided to a G2-Si HDMS mass spectrometer with ion mobility separation (Waters), ionized with an electrospray ionization source (capillary temperature 250°C, spray voltage 3.0 kV) and mass spectra acquired in positive ion mode over a range of 50–2000 *m/z* in $HDMS^E$ or HDMS mode for nondeuterated and deuterated samples, respectively. [Glu1]-Fibrinopeptide B standard (Waters) was employed for lock-mass correction. During chromatographic separation of the peptide mixtures, the pepsin column was washed three times with 80 μl each of 4% (v/v) acetonitrile + 0.5 M guanidine hydrochloride and blank injections performed between each sample. All measurements were carried out in triplicate.

Peptide identification and analysis of deuterium incorporation were carried out with ProteinLynx Global SERVER 3.0.1 (PLGS, Waters) and DynamX 3.0 softwares (Waters) as described previously [60].

Bacterial strains for efficiency of transformation assay

The vector pRSFDuet-1 containing the Type IF2 CRISPR–Cas proteins (pCas2-3f2, Cas5, Cas6, and Cas7 WT) was transformed into an *E. coli* BL21-AI strain along with a pCDFDuet-1 plasmid containing a crRNA fragment that spacer targets the ampicillin gene (pCRISPR Anti-AmpR) with a GG–PAM in a pETDuet-1 plasmid (see Table 3). This strain was used as a positive control of the assay and represents an active system.

Table 3. Key resources table

Reagent or resource	Source	Identifier
Bacterial and virus strains		
Escherichia coli BL21 (DE3) competent cells	Novagen	Cat# 69450-M
Escherichia coli BL21 (DE3)—pLysS competent cells	Novagen	Cat# 69451-M
Chemicals, peptides, and recombinant proteins		
AMP–PNP	Roche	Cat# 10102547001
DTT	Roche	Cat# DTT-RO
$MgCl_2$	Sigma–Aldrich	Cat# 208337
HEPES	Carl Roth	Cat# 6763
Sodium chloride	Carl Roth	Cat# HN00
Potassium dihydrogen phosphate	Carl Roth	Cat# 3904
Phosphoric acid	Carl Roth	Cat# 6366
Guanidine hydrochloride	Carl Roth	Cat# 6069
Formic acid	AppliChem	Cat# A0748
Acetonitrile	Thermo Fisher	Cat# A/0627/17
Sodium hydroxide	Thermo Fisher	Cat# S/4920/60
Hydrochloric acid	Carl Roth	Cat# 4625
[Glu1]-Fibrinopeptide B standard	Waters	Cat# 700004729
Deuterium oxide	Deutero	Cat# 00506
Porcine pepsin	Sigma–Aldrich	Cat# 10108057001
POROS 20 R2	Thermo Fisher	Cat# 1112906
Deposited sata		
R-loop–Cas3–Cascade Type I-F2 model	This study	PDB: 9G44
R-loop–Cas3–Cascade Type I-F2 cryo-EM volume	This study	EMD: 51023
HDX-MS data have been deposited to the ProteomeXchange Consortium via the PRIDE [62] partner repository with the dataset identifier PXD068253		
Oligonucleotides		
R-loop, target: GCGAGGAGGGGAGGTTATAG-GTTTGCGCGTCTTGCTGGGCGATAGGTGGCACGTGGG	Sigma–Aldrich	n/a
R-loop, nontarget: CCCACGTGCCACCATCATTATTATTGTTATTATTCT-TAGTATTATTCCCCTCCTCGC	Sigma–Aldrich	n/a
cas3 fwd: TTAAGGTCTCCCATGGGCCACCATCACCATCACCATATGGT-GACATTCATCAGTCAGTGC	Sigma–Aldrich	n/a
cas3 rev:TTAAGGTCTCCTCGAGTTCCTCATCTTCAGTGGTTTGATTAATTTG	Sigma–Aldrich	n/a
pUC19-AarI fwd: ATTACACCTGCTATACTGCTGCCACCGCTGAG	Sigma–Aldrich	n/a
pUC19-AarI rev: TATACACCTGCATTACAAAATTATTTCTACAGGGGAATTG	Sigma–Aldrich	n/a
R1 fwd: TTTGGTTCACCGCCGCACAGGCGGCTTAGAAACGAGACCGGGATGC	Sigma–Aldrich	n/a
R1 rev: AGGTGCATCCCGGTCTCGTTTCTAAGCCGCCTGTGCGGCGGTGAAC	Sigma–Aldrich	n/a

Table 3. Continued

Reagent or resource	Source	Identifier
R2 fwd: ACCTCCCGAAGGGGTCTCGTTCACCGCCGCACAGGCGGCTTAGAAA	Sigma–Aldrich	n/a
R2 rev: GCAGTTTCTAAGCCGCCTGTGCGGCGGTGAACGAGACCCCTTCGGG	Sigma–Aldrich	n/a
Spacer “24” fwd: GAAAAGTCACAGAAAAGCATCTTACGGCTGGCATGAG	Sigma–Aldrich	n/a
Spacer “24” rev: TGAACTCATGCCAGCCGTAAGATGCTTTTCTGTGACT	Sigma–Aldrich	n/a
Spacer “25” fwd: GAAAAGTCACAGAAAAGCATCTTACGGAGGGCATGAG	Sigma–Aldrich	n/a
Spacer “25” rev: TGAACTCATGCCCTCCGTAAGATGCTTTTCTGTGACT	Sigma–Aldrich	n/a
Spacer “26” fwd: GAAAAGTCACAGAAAAGCATCTTACGGATTGCATGAG	Sigma–Aldrich	n/a
Spacer “26” rev: TGAACTCATGCAATCCGTAAGATGCTTTTCTGTGACT	Sigma–Aldrich	n/a
Spacer “27” fwd: GAAAAGTCACAGAAAAGCATCTTACGGATGTCATGAG	Sigma–Aldrich	n/a
Spacer “27” rev: TGAACTCATGACATCCGTAAGATGCTTTTCTGTGACT	Sigma–Aldrich	n/a
Spacer “28” fwd: GAAAAGTCACAGAAAAGCATCTTACGGATGGAATGAG	Sigma–Aldrich	n/a
Spacer “28” rev: TGAACTCATTCCATCCGTAAGATGCTTTTCTGTGACT	Sigma–Aldrich	n/a
Spacer “29” fwd: GAAAAGTCACAGAAAAGCATCTTACGGATGGCCTGAG	Sigma–Aldrich	n/a
Spacer “29” rev: TGAACTCAGGCCATCCGTAAGATGCTTTTCTGTGACT	Sigma–Aldrich	n/a
Spacer “24 + 25” fwd: GAAAAGTCACAGAAAAGCATCTTACGGCGGGCATGAG	Sigma–Aldrich	n/a
Spacer “24 + 25” rev: TGAACTCATGCCCGCCGTAAGATGCTTTTCTGTGACT	Sigma–Aldrich	n/a
Spacer “25 + 26” fwd: GAAAAGTCACAGAAAAGCATCTTACGGAGTGCATGAG	Sigma–Aldrich	n/a
Spacer “25 + 26” rev: TGAACTCATGCACTCCGTAAGATGCTTTTCTGTGACT	Sigma–Aldrich	n/a
Spacer “26 + 27” fwd: GAAAAGTCACAGAAAAGCATCTTACGGATTTCATGAG	Sigma–Aldrich	n/a
Spacer “26 + 27” rev: TGAACTCATGAAATCCGTAAGATGCTTTTCTGTGACT	Sigma–Aldrich	n/a
Spacer “27 + 28” fwd: GAAAAGTCACAGAAAAGCATCTTACGGATGTAATGAG	Sigma–Aldrich	n/a
Spacer “27 + 28” rev: TGAACTCATTACATCCGTAAGATGCTTTTCTGTGACT	Sigma–Aldrich	n/a
Spacer “28 + 29” fwd: GAAAAGTCACAGAAAAGCATCTTACGGATGGACTGAG	Sigma–Aldrich	n/a
Spacer “28 + 29” rev: TGAACTCAGTCCATCCGTAAGATGCTTTTCTGTGACT	Sigma–Aldrich	n/a
H156A fwd:AGGTTGCTTGGCGGATTTAGGGAAAATTGAC	Sigma–Aldrich	n/a
H156A rev:GCAATAAAATTCGCAATTG	Sigma–Aldrich	n/a
K827E fwd:CAACAAAGATGAAAAACGCACCAAG	Sigma–Aldrich	n/a
K827E rev:TTCTTTGGTGGAACGGTAATAG	Sigma–Aldrich	n/a
Q889E fwd:TGGTTATGACGAAAGCGATAAAGATTTAC	Sigma–Aldrich	n/a

Table 3. Continued

Reagent or resource	Source	Identifier
Q889E rev:CAAATAGCCTTGGTGGCG	Sigma–Aldrich	n/a
Q507A fwd:CACCATAGATGCGATTCTTGGTTCAGTG	Sigma–Aldrich	n/a
Q507A rev:GTGAGCACTATATCGCCG	Sigma–Aldrich	n/a
D532A fwd:TGTAGTGTTTGCGGAGTTCCATGAATAC	Sigma–Aldrich	n/a
D532A rev:TGCACATTTAAAAAATCGATAAG	Sigma–Aldrich	n/a
H353A fwd:TGATGAGTTCGCGGAATACGTCAACATGCC	Sigma–Aldrich	n/a
H353A rev:AACACTACATGCACATTTAAAAAATC	Sigma–Aldrich	n/a
Recombinant DNA		
Expression of protein components of Cascade Type I-F2: plasmid: pRSFDuet1	This study	n/a
Expression of crRNA: plasmid: pCRISPR-18	[43]	n/a
Expression of protein Cas3: plasmid: pET24d	This study	n/a
Expression of protein components for EoT experiments (Cas2-3f2, Cas5, Cas6, Cas7): plasmid: pRSFDuet1	This study	n/a
Software and algorithms		
COOT v0.9.7	[57]	https://www2.mrc-lmb.cam.ac.uk/personal/pemsley/coot/; RRID: SCR_014222
PHENIX v1.19.2	[59]	https://www.phenix-online.org; RRID: SCR_014224
UCSF Chimera v1.16	[55]	https://www.cgl.ucsf.edu/chimera; RRID: SCR_004097
RELION5.0	Scheres	http://www2.mrc-lmb.cam.ac.uk/relion; RRID: SCR_016274
CTFFIND4	[53]	http://grigoriefflab.janelia.org/ctffind4; RRID: SCR_016732
MotionCor2	[52]	https://emcore.ucsf.edu/ucsf-software
SerialEM4.0.9	[50]	n/a
DynamX 3.0	Waters	https://www.waters.com/nextgen/de/de/library/library-details.html?documentid=720005145&t=waters-DynamXHDXDataAnalysisSoftware-720005145
PLGS 3.0.1	Waters	https://www.waters.com/waters/en_US/ProteinLynx-Global-SERVER-(PLGS)/nav.htm?cid = 513821&locale = en_US
Other		
HisTrap HP column	Cytiva	Cat# GE17-5248-01
Amicon concentrators (50 kDa)	Millipore	Cat# UFC905024
Superdex 200 increase 10/300 GL column	Cytiva	Cat# GE28-9909-44
Quantifoil R 2/2 on 300 copper mesh	Quantifiol	https://www.quantifoil.com/products/quantifoil/quantifoil-circular-holes
ACQUITY UPLC BEH C18 1.7 μm 1.0 × 100 mm	Waters	Cat# 186002346

The negative control was the same strain containing pCas2-3f2 WT, but with a crRNA targeting Anti-AmpR with a different PAM sequence rendering the system inactive. Similarly, six strains were transformed with a Cas2-3f2 gene carrying the following point mutations: K827E, Q889E, Q507A, H157A, D532A, H535A. The strains containing the mutations were transformed with the pCRISPR Anti-AmpR for the efficiency of transformation (EoT) assays. Mutations were introduced using a QuickChange site-directed mutagenesis kit (New England Biolabs) following the manufacturer's protocol (see Table 3).

Preparation of electrocompetent cells and efficiency of transformation assays

Aliquots of fresh overnight cultures from the six strains containing the mutations and the respective controls were inoculated in 20 ml of LB medium supplemented with kanamycin (25 μg/ml) and spectinomycin (25 μg/ml). All cultures were normalized to yield a final culture with an optical density at 600 nm (OD_{600}) of 0.1. Cultures were grown until OD_{600} = 0.3. Subsequently, protein expression was induced by adding 0.1 mM of IPTG and 0.2% (w/v) of arabinose. Once an OD_{600} of 0.6 was reached, cells were pelleted in pre-cooled Falcon tubes centrifuged at 4600 × *g* for 8 min at 4°C. Pellets were washed twice with cold double-distilled water (ddH_2O) and centrifuged again. Finally, pellets were resuspended in 200 μl of ddH_2O, from which 50 μl were taken and combined with 5 ng of the target plasmid (pETDuet-1). Each mixture was transferred to pre-cooled 0.1-cm electroporation cuvettes and exposed to one pulse at 1.8 kV, 25 μF, and 200 ohms (Biorad electroporator). Transformation mixtures were immediately supplemented with 550 μl of LB medium and transferred to a 1.5-ml Eppendorf tube and recovered for 1 h at 37°C with shaking at 400 rpm. Finally, 100 μl were plated on LB agar plates containing ampicillin (50 μg/ml), kanamycin (25 μg/ml), and spectinomycin (25 μg/ml). After overnight incubation at 37°C, the number of colonies per plate was counted and the % of EoT was calculated as the ratio between the colony count for the strain of interest and the colony count for the negative control (CFU treatment/CFU negative control∗100). EoT assays were performed in triplicate and error bars were calculated as standard error of the mean.

Results

Cryo-EM structure of the DNA and Cas3-bound Type I-F2 Cascade

To determine the structural basis for Cas3 recruitment, we focused on the Type I-F2 complex from *S. putrefaciens* CN32 (Fig. 1A), for which "crRNA-shortened" Cascade structures in the absence and presence of DNA are available [24]. The purified "full-length" Cascade was complexed with double-stranded (ds)DNA containing a crRNA spacer complementary TS (Fig. 1B); to favor R-loop formation, the DNA lacked complementarity between the NTS and TS in the spacer region (Fig. 1C). Subsequently, a Cas2-truncated variant of Cas2-3f2 (CasΔ2–3f2, hereafter referred to as Cas3), which cannot form the Cas2-3f2 dimer [63], was added in the absence of ATP. By omitting ATP and including Mg^{2+} ions, we could successfully stall the helicase, allowing us to capture Cas3 bound to Cascade in a helicase state. Cryo-EM structure determination revealed the Type I-F2 complex in the presence of DNA and Cas3 at an overall resolution of ∼3.2 Å (Fig. 1D, Table 1, and Supplementary Fig. S1).

Our model reveals a crescent shaped Cascade with overall dimensions of 200 × 130 × 90 Å, with subunits that compare well with our previous structures of the "shortened" Type I-F2 Cascade complex bound to a cognate DNA target (Fig. 1D and E, and Supplementary Fig. S2). Briefly, our model includes well-resolved crRNA, TS, and NTS at local resolutions ranging from 3.2 to 5.2 Å. In contrast, the PAM-distal region of the DNA duplex was poorly resolved, likely due to increased flexibility (Fig. 1D and E, and Supplementary Fig. S3). A fully resolved Cas5 at a resolution of ∼3.5–5 Å, associated to the 5′ end of the crRNA, as well as six Cas7 copies assembled along the crRNA at a resolution of ∼3.5 Å and Cas6, bound to the 3′ crRNA hairpin loop, less well resolved at ∼5 Å. Strikingly, we found Cas3, resolved at ∼4.5 Å, recruited to the Cas7 backbone and Cas5 at the center of the Cascade complex (Fig. 1D and E, and Supplementary Fig. S3).

This structure provides the first high-resolution structure of a complete DNA- and Cas3-bound Type I-F2 Cascade complex. These findings reveal the structural basis for Cas3 recruitment in Type I-F2 systems, showing that Cas3 docks centrally onto the Cascade complex through coordinated interactions with Cas7 and Cas5. Unlike in other Type I systems (Type I-C and I-E) where Cas3 is recruited externally via the large subunit (Cas8), the Type I-F2 system employs a more integrated architecture, using the Cas7–Cas5 interface for Cas3 engagement.

Cas7 and Cas5 identify the DNA target

Preceding the recruitment of Cas3, Type I-F2 recognizes the PAM to subsequently unwind the downstream DNA target. Hybridization of the crRNA and TS for sequence interrogation then leads to formation of the R-loop [28]. Mirroring the DNA interactions observed in our X-ray crystal structure of the "short" Type I-F Cascade [24], Cas5 and Cas7 mediate PAM recognition and target sequence identification, respectively. In brief, our cryo-EM structure confirmed that the GG–PAM is recognized solely by Cas5 (Fig. 2A and B). For PAM sequence recognition, Cas5 extends an α-helical (AH) domain across the double-stranded PAM-motif to probe the base pair identity via amino acids glutamine 113 and lysine 253 (Fig. 2B and Supplementary Fig. S4). Notably, we found the G/C PAM base pair in position 0 paired up, in contrast to our previous X-ray structure, where the G/C base pair was distorted by glutamine 113 (Supplementary Fig. S4). We have previously shown that the AH domain rearranges upon DNA binding (∼10 Å), suggesting that different conformational states might account for this observation. Superimposition of DNA-bound Cas5 (this study) with Cas5 in the absence or presence of DNA from our previous study revealed rearrangements in the AH domain (Supplementary Fig. S2), where α-helix 5 and the adjacent loop around asparagine 205 close in on the PAM.

Downstream of the PAM, NTS, and TS bifurcate to hybridize TS and crRNA for target sequence recognition (Fig. 2C). Parallel to the crRNA:TS hybrid, the single-stranded NTS is guided along a positively charged trench formed by the wrist loops of Cas7 (Fig. 2D). The NTS is guided only up to the third Cas7 (Cas7.3) subunit before a 90° kink, induced by the glutamine 889, positions the NTS for handover to Cas3 (Fig. 2E).

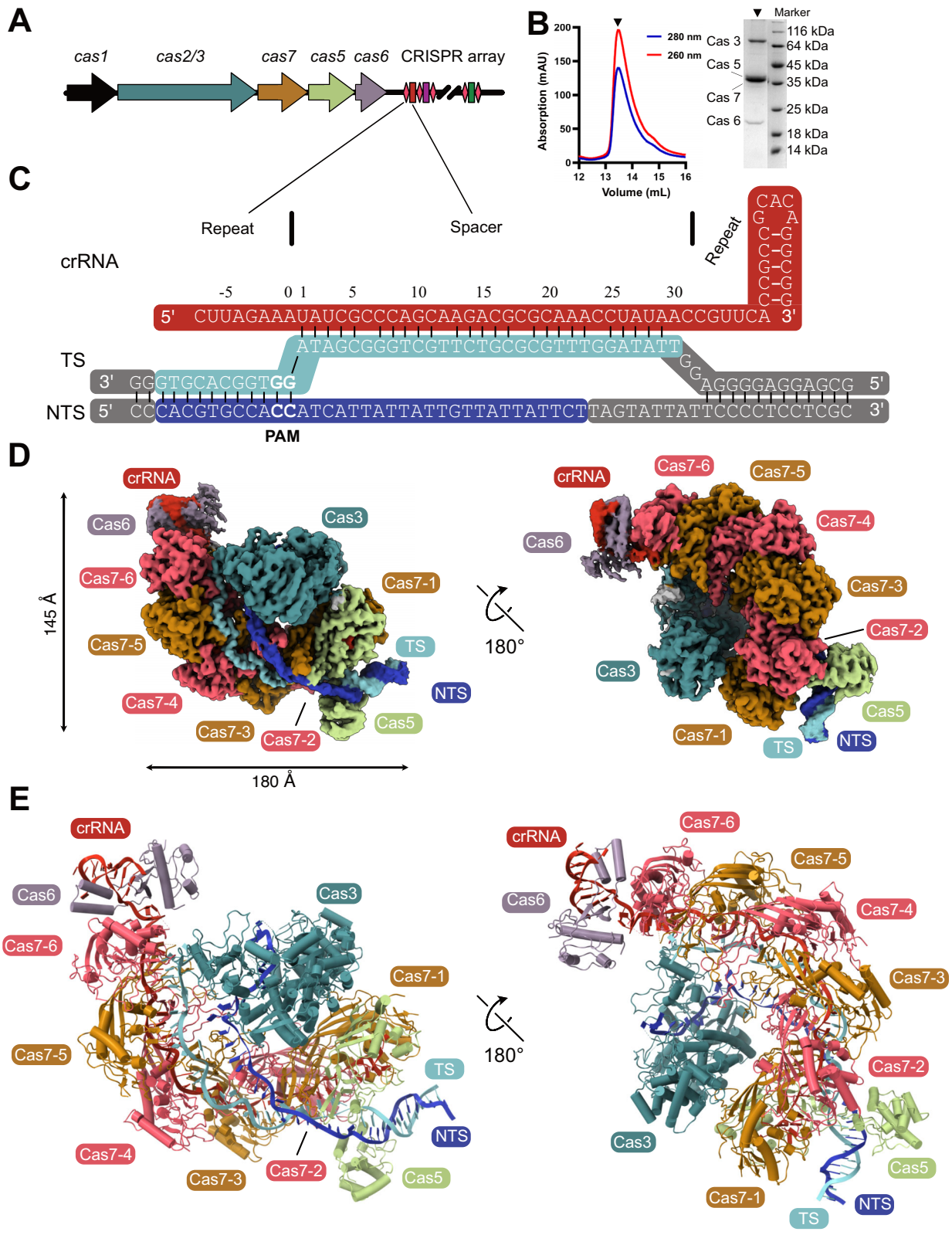

Figure 1. Type I-F2 forms a compact DNA-interference effector complex. (**A**) CRISPR–Cas locus of the Type I-F2 system from *S. putrefaciens* CN32. (**B**) SEC profile and SDS–PAGE analysis of the purified Cascade–Cas3 complex; the triangle indicates the fraction used for cryo-EM. (**C**) Sequences of crRNA, TS, and NTS used for assembly of the Cascade R-loop complex; gray shading marks regions not resolved in the structure. (**D**) Cryo-EM density map of the Cascade–Cas3 complex, with subunits colored according to the scheme in panels (A) and (C). (**E**) Atomic model of the Type I-F2 Cascade–Cas3 complex.

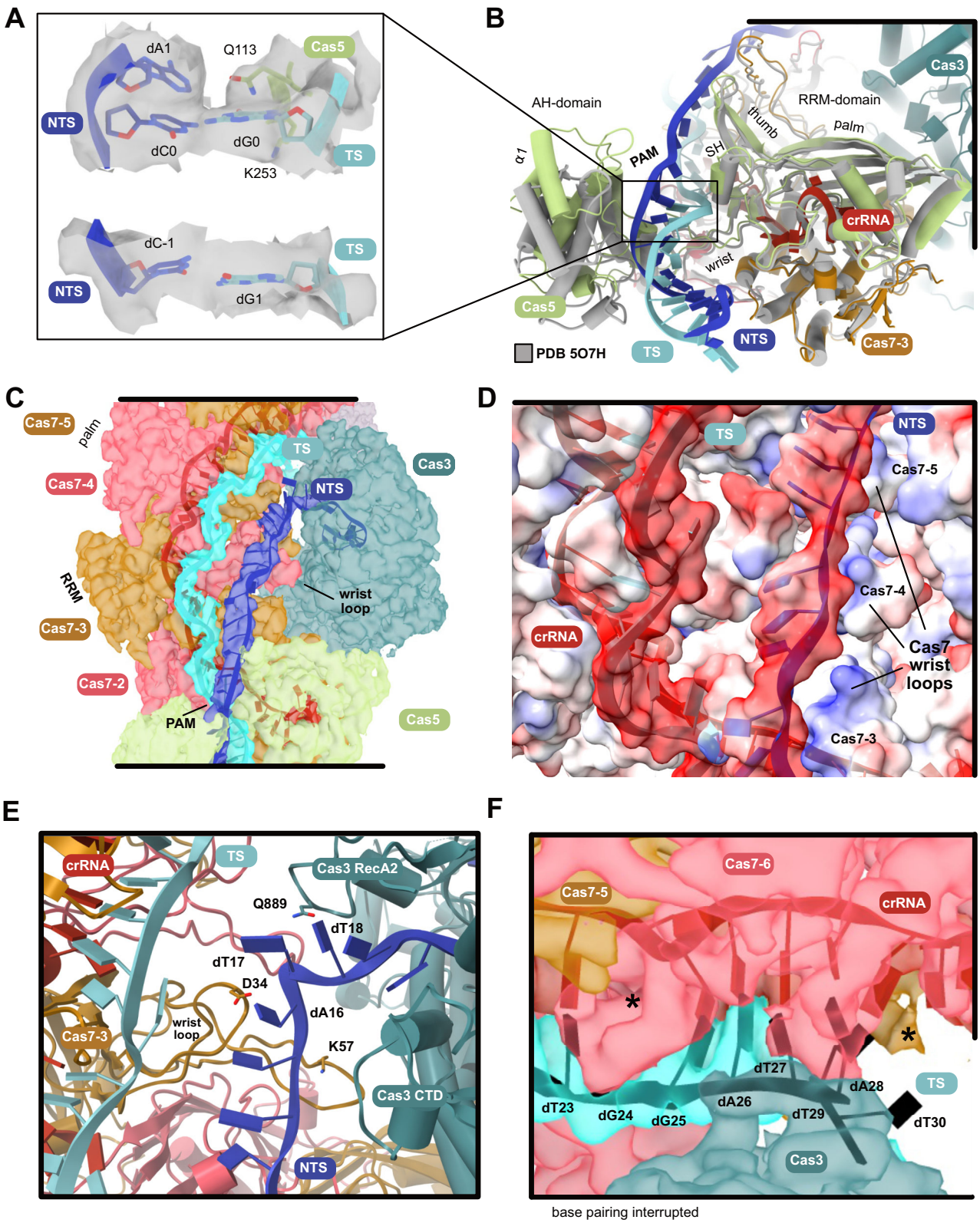

Figure 2. Recognition of TS and NTS. (**A**) The PAM base pairs dC-1/dG1 and dC0/dG0 with the respective electron map in 2 Å proximity. Glutamine 113 interferes with the base pairing of dC0/dG0, leading to a split of TS and NTS. (**B**) Close up on Cas5 bound to the PAM. Comparison of Cas5 from this study (olive) to Cas5 in minimal Type I-F2 without R-loop (gray; PDB: 5O7H) reveals the reorganization of the AH domain and the thumb of the RRM domain. (**C**) Path of the crRNA, TS, and NTS after the R-loop. crRNA and TS are guided by the RRM pockets of Cas7 subunits, while the NTS is complexed by lysine-rich thumbs. (**D**) The single-stranded NTS is guided along a positively charged trench formed by the wrist loops of Cas7-3, 4, 5. (**E**) Rerouting of the NTS toward Cas3 by a glutamine 889-induced 90° kink causes the NTS to pass between the RecA1 and CT-domains of Cas3. (**F**) PAM-distal TS with base pairing in the Cas7.6–Cas3 contact zone. Regular interruptions of the TS–crRNA base pairing are marked with an asterisk.

As a result of the duplex traversing the thumb motif of Cas7, one in six TS base is not paired with its complementary crRNA base (Fig. 2F). At the PAM distal segment of the crRNA:TS hybrid, close to Cas6, the duplex is capped by the thumb motif of the distal Cas7.6 at base pair 28. In turn, the remaining portion of TS complementary to crRNA is guided away from the complex and was thus not resolved in our structure, likely due to flexibility (Fig. 2F).

Together, these findings reveal that in Type I-F2 systems, Cas5 and Cas7 coordinate DNA sequence interrogation, with Cas5 responsible for PAM specificity and Cas7 guiding the crRNA:TS hybrid and single-stranded NTS. The observed AH domain rearrangements in Cas5 underscore a potential allosteric switch that may fine-tune PAM engagement. These mechanistic insights highlight how Type I-F2 achieves efficient R-loop formation and substrate handover in the absence of the large subunit Cas8.

Cas3 is guided to the NTS via cas7 and cas5

In the evolutionarily related Types I-E and I-F1 Cascades, DNA binding triggers a conformational change in Cas8 for the recruitment of Cas3 [41]. To understand how Type I-F2 binds Cas3 upon R-loop formation, we analyzed the interactions between Type I-F2 Cascade and Cas3.

Cas3 is a helicase–nuclease effector enzyme composed of four domains (Fig. 3A). The helicase core of Cas3 is composed of RecA1 and RecA2, which are fused to an N-terminal metal ion-dependent HD nuclease domain and a C-terminal accessory domain (CTD). The CTD is likely involved in single-stranded DNA recruitment and allosteric regulation of Cas3 [21, 38]. In our structure, all four domains engage in interactions with the Cascade. PAM-proximally, RecA1 interacts with Cas5, and the HD domain interacts with Cas7.1 (Fig. 3B). This interface is shaped by the interaction of Cas5 lysine 335 with Cas3 aspartate 584 and glutamate 416, as well as a contact between Cas7.1 glutamate 303 and Cas3 lysine 215. Additionally, Cas7.1 serine 298 and glutamate 299 lie in close proximity of Cas3 asparagine 143. Along the Cas7 backbone, the RecA2 domain and CTD of Cas3 interact with the Cas7 wrist loop NTS-trench (Fig. 2D). Here, the contact is mediated via the NTS, with aspartate 34 and lysine 57 being the main guiding residues of Cas7.3. Lysine 740 coordinates the NTS backbone, while glutamine 889 forms hydrogen bonds to the bases. At the PAM-distal crRNA:TS hybrid, the CTD domain contacts the RRM of Cas7.6 (Fig. 3C). Serine 123 of Cas7.6 and asparagine 904 of Cas3 form a hydrogen bond, while serine 124 of Cas7.6 contacts the backbone of Gly942.

These results define a unique recruitment mechanism for Cas3 in Type I-F2 systems, where coordinated multivalent contacts with both Cas5 and several Cas7 subunits position Cas3 for docking along the NTS path. Unlike Type I-E and I-F1 systems that rely on the large subunit (Cas8) for Cas3 recruitment, Type I-F2 compensates for the absence of a large subunit through a distributed interaction network involving the Cas7 backbone, Cas5, and the NTS itself. This mode of recruitment reflects a structurally integrated handover process, coupling R-loop formation with immediate Cas3 engagement. It highlights a functionally compact yet highly specialized architecture for interference that is distinct from other Type I systems and suggests evolutionary streamlining of effector loading in Type I-F2.

Structural dynamics of Type I-F2-mediated DNA interference

Structural rearrangements in Cascade complexes are known to play a key role in signalling for Cas3 recruitment upon target binding [64, 65]. To investigate conformational changes associated with target recognition and Cas3 recruitment, we performed HDX-MS, in the presence of AMPPNP, across four defined states of the Type I-F2 interference complex: (I) apo Cascade, (II) Cascade bound to R-loop DNA, (III) Cascade–R-loop in complex with Cas3, and (IV) apo Cas3 alone (Fig. 4A and Supplementary Figs S5 and S6).

Comparing states (I) and (II) revealed the structural dynamics associated with R-loop formation. While Cas6 exhibited no changes in hydrogen–deuterium exchange, pronounced HDX protection was observed in three loop regions of Cas7 (Fig. 4B and Supplementary Fig. S5), indicating a stabilization of the elements consistent with direct engagement of the crRNA-bound TS. Significant HDX reductions were also detected in Cas5, particularly around the PAM-binding groove, corroborating its critical role in target recognition. In contrast, the C-terminal tail and finger loop of Cas7 remained largely unaffected by DNA binding. We next compared states (II) and (III) to assess the structural reorganization of Cascade/R-loop upon Cas3 recruitment, however, no further changes in the conformation of Cascade proteins were apparent by HDX-MS (Fig. 4C). We assume that this is due to the interaction primarily being mediated by side-chain interactions between Cas3 and Cas7 in particular whereas HDX-MS tracks changes in accessibility of the peptide backbone amide protons. This is conceivably compounded by the repetitive nature of Cas7 within the Cascade complex as HDX-MS does not provide Cas7 subunit-specific resolution.

Nevertheless, and consistent with our cryo-EM structure, strong HDX protection of Cas3 was observed in comparison of Cascade/R-loop-engaged Cas3 (state III) and Cas3 in isolation (state IV; Fig. 4C), validating the stability of the interaction in solution. Specifically, Cas3 HDX reduction was apparent at the Cas7.1 and Cas7.6 interaction interfaces as well as several portions within the RecA1 and RecA2 domains, all of which partake in NTS recognition (Fig. 4C and Supplementary Fig. S6B). Notably, HDX protection extended into Cas3's helicase channel along the NTS path consistent with substrate engagement for processive DNA unwinding. The Cas3 C-terminal domain in particular exhibited widespread protection from deuterium exchange in the Cascade/R-loop-bound state in consequence of Cas3 CTD insertion in between the Cascade-coordinated TS and the Cas3 helicase domain-directed NTS. This further suggests that the CTD may traverse from a more dynamic state in solution to a more ordered conformation within the complex. This behavior is consistent with our biochemical observations of Cas3 instability in the absence of Cascade and may point to an additional, yet unexplored, regulatory role of the CTD in effector complex assembly or activity.

Cas3 and PAM-distal mismatches

Notably, at the PAM-distal crRNA:TS hybrid, the CTD domain of Cas3 is positioned in proximity to the base pairs at position 24–28 (Fig. 3C). To understand whether PAM-distal

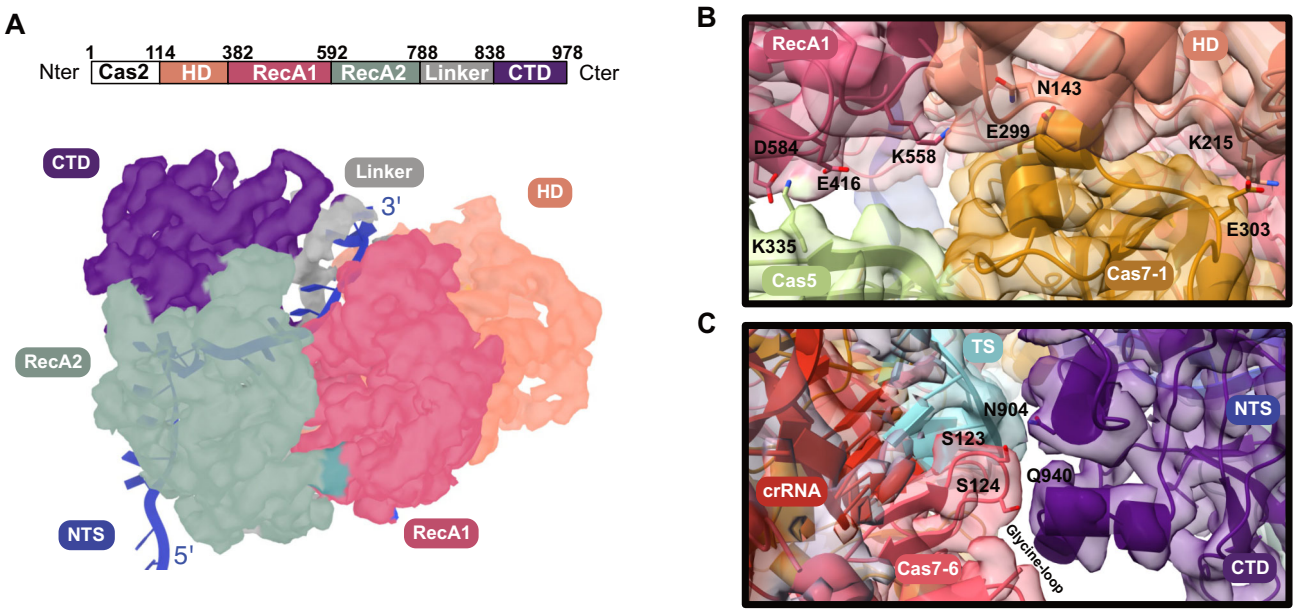

Figure 3. Recruitment of Cas3. (**A**) Cryo-EM map of the domain architecture of Cas3 with route of the NTS shown in cartoon representation. (**B**) Interface between Cas3 and Cas5/Cas7-1. (**C**) Interface between Cas7-6, Cas3, and the TS.

crRNA:TS hybrid formation is critical for Cas3-mediated DNA-interference, we employed an *in vivo* EoT assay in *E. coli* [24]. In brief, *E. coli* expressing the Type I-F2 *cas* operon heterologously along fully matched or mismatched beta-lactamase (*bla*) targeting guides, was transformed with a plasmid encoding *bla*, prior to selection with ampicillin (Fig. 5A). The assay revealed increased transformation efficiencies when individual mismatches were present in base pairs 25, 27, and 29, suggesting that mismatches may influence the DNA-interference activity (Fig. 5A). Next, we introduced double mismatches, which, to our surprise, were relatively well tolerated (Fig. 5A). Together, these observations suggest that interference efficiency in the PAM-distal region may be influenced by the conformation of the crRNA:TS hybrid adjacent to the Cas3 CTD. Single mismatches in this region may perturb the local hybrid conformation in a manner that is unfavorable for Cas3 recruitment and activation, or for proper positioning of the DNA substrate for downstream engagement. In contrast, certain double mismatches could alter the hybrid conformation in a way that remains compatible with Cas3 association and subsequent strand handover. Thus, our data are consistent with a model in which Cas3 engagement is sensitive to the overall conformation of the crRNA:TS hybrid.

Intrigued by the interaction of Cas3 with the PAM-distal crRNA:TS hybrid and terminal Cas7.6 subunit, we wondered whether the interactions are important for Cas3 recruitment. We have previously shown that deletion of multiples of 6 nucleotides of the crRNA spacer allows for shortening of the Cascade complex by removing Cas7 binding sites, while simultaneously abrogating DNA-interference activity [24, 27]. Heterologous expression and purification of Cascade complexes, followed by incubation with shortened versions of TS–NTS bubbled DNA and Cas3, showed the same capability to form the effector complex as full-length TS (Supplementary Fig. S7).

Together, these data demonstrate that while PAM-distal mismatches cause defects in the interference activity of Cas3, the interface formed between Cas3's CTD, the PAM-distal crRNA:TS hybrid, and Cas7.6 may not be essential for Cas3 recruitment. This observation suggests that the interactions between Cas3 and the PAM-proximal Cas5 and Cas7 subunits are sufficient to promote Cas3 binding, but not to license DNA-interference.

Four Cas3 domains cooperate to guide and degrade the NTS

To evaluate the role of specific Cas3 residues in DNA degradation, we employed our EoT interference assay. Cas3-mediated, HD-dependent DNA degradation is a well-established biochemical hallmark of Type I systems [66], and our EoT assays therefore provide a stringent *in vivo* readout of Cas3 activity, directly linking interference efficiency to Cas3 catalytic function.

Point mutations in Cas3 showed varying effects, depending on how critical each residue is for DNA processing (Fig. 5B). Residues Q889 and Y887 are in close proximity with bases 16 and 17 of the NTS, helping guide it into Cas3 (Fig. 2D and Supplementary Fig. S8). Mutating Q889 to glutamate did not impair function. The NTS is then channelled between the CTD and RecA2 domains, with residues K652, S651, and K658 coordinating the phosphate backbone, and K892, M629, N841, and R838 contacting the bases (Supplementary Fig. S8). Before reaching the HD nuclease domain, the NTS is twisted and further stabilized by RecA1 residue Q507 and CTD residues K827, K831, and K834 (Supplementary Fig. S8). Individual mutations at K827 and Q507 did not disrupt the activity in the EoT assay. These data show that Cas3 robustly engages the NTS for interference.

Together, the RecA1, RecA2, and CTD domains form a clamp that guides the NTS into the HD domain for cleavage. The CTD acts like a sliding ramp, while RecA1 and RecA2 help feed the DNA into the catalytic core. Since RecA1 and RecA2 are ATP-dependent helicase domains, we tested mutations in conserved Walker A and Walker B motifs. Mutation

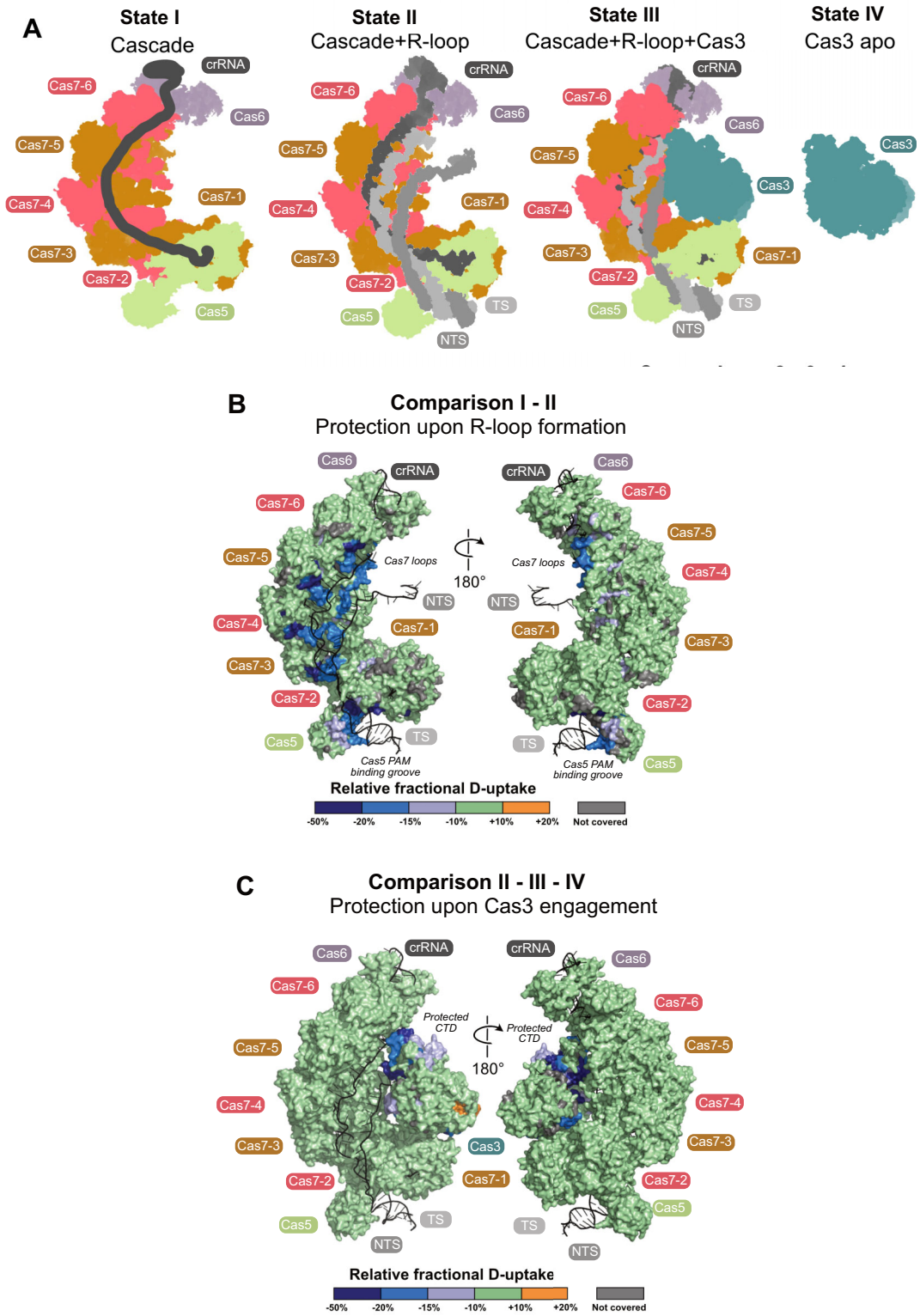

Figure 4. Dynamics of effector complex assembly. (**A**) Different states of the effector complex probed with HDX. (**B**) Changes in HDX between states I and II mapped on a surface representation of the Cascade complex. The color scale indicates the relative fractional deuterium uptake (ΔRFU), representing the difference in exchange between the two states, normalized to the theoretical maximum. Cool colors indicate regions that become more protected (lower uptake) upon DNA binding, whereas warm colors highlight regions that become more flexible or solvent-exposed (higher uptake). (**C**) HDX changes upon Cas3 recruitment to the binary complex depicted on a surface representation of the effector complex.

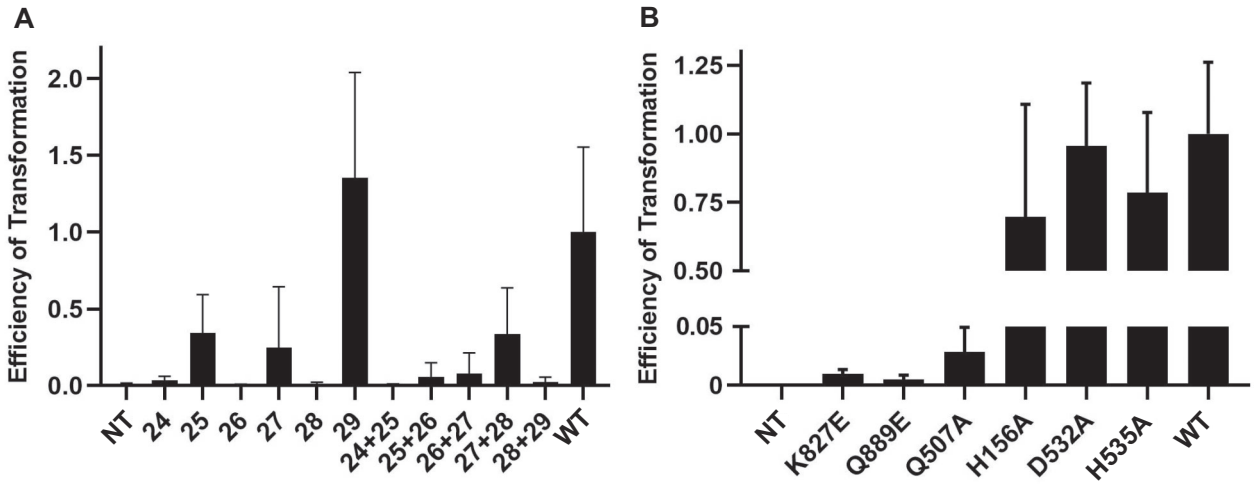

Figure 5. EoT assays. (**A**) EoT assay with crRNA mismatches introduced at bases corresponding to the numbers on the *x*-axis. "+" refers to the nontargeting variant, "-" is the wild-type control. (**B**) EoT with mutations introduced into Cas3 reveal a small impact of residues involved in NTS coordination. Mutations within the Cas3 nuclease abolish its activity.

of H535A, the invariant lysine of the Walker A/P-loop motif (GxxxxGK[ST]) (GxxxxGK[ST]) responsible for ATP binding, completely abolished activity (Fig. 5B). Likewise, D532A, which maps to the Walker B motif, critical for coordinating Mg^{2+} and ATP hydrolysis (Supplementary Fig. S8), also eliminated interference (Fig. 5B). In addition, mutation of H156A in the HD nuclease domain disrupted DNA cleavage entirely (Fig. 5B), supporting a coordinated mechanism of ATP-driven strand translocation and cleavage.

These results confirm that the action of the helicase and CTD domains is essential for NTS threading and degradation. The DNA-binding channel formed by these domains ensures accurate strand positioning, and disruption of key catalytic residues halts interference entirely, emphasizing the conserved ATP-driven mechanism of Cas3-mediated DNA degradation.

Cas3 is recruited in the helicase active conformation

Previous studies have revealed structures of *in trans* or constitutively recruited Cas3 bound to the R-loop Cascades in Types I-E and I-A, respectively [14, 22, 41, 67]. In brief, Type I-A Cascade initially recruits Cas3 in an inactive state in the absence of DNA. Only after the R-loop is fully formed is Cas3 activated allosterically and proceeds to nick and degrade the NTS. In contrast, Cas3-Cascade association in Type I-E systems is triggered by the formation of the R-loop. This induces a conformational change in Cas8, enabling the recruitment of Cas3 *in trans* to nick the NTS, as observed in the structure of Xiao *et al.* [22]. The progressive degradation of the NTS is then thought to be carried out in an ATP-dependent, helicase-mediated manner independent of the Cascade complex.

The helicase/nuclease Cas3 typically consists of four subdomains to fulfil its task of unwinding and degrading ssDNA (Fig. 3A). The two SF2 helicase domains (RecA1 and RecA2) are separated by a cleft, which harbors the ATP binding site unoccupied in our structure (Supplementary Fig. S8). Opposite to this, the CTD acts as a sliding ramp that guides the displaced NTS toward the HD nuclease domain. Nuclease activity is metal dependent and is typically supported by Mg^{2+} or Mn^{2+} ions [68]. Although Fe^{2+} has been observed in some crystal structures, these states are catalytically inactive and likely reflect non-physiological metal coordination [68]. Our use of Mg^{2+}-containing purification buffers therefore represents a functional substitution for the natural divalent cofactors.

In our structure, we observe Cas3 recruited to the Cascade, while at the same time threading the NTS through the cleft between RecA1, RecA2, and CTD, as observed in the helicase conformations reported by Huo *et al.* [68] (Supplementary Fig. S9). In these crystal structures of I-E Cas3 in the absence of Cascade, ssDNA could be traced into the HD-domain, where it appeared to be hydrolyzed. However, in our structure, the NTS wraps around the CTD completely and exits Cas3 on the PAM distal site.

Discussion

Structural reduction and mechanistic divergence of interference in type I-F2 CRISPR–Cas systems

Type I CRISPR–Cas systems use multisubunit Cascade complexes to monitor DNA and recruit the helicase–nuclease Cas3 for target degradation. In most characterized subtypes, including Type I-E and Type I-F1, this process is tightly coordinated through a large subunit (Cas8), which mediates PAM recognition and controls the activation and recruitment of Cas3. In contrast, our structure of the minimal Type I-F2 Cascade from *S. putrefaciens* reveals a divergent architecture that functions independently of Cas8, suggesting a fundamentally different mechanism of DNA interference.

The Type I-F2 Cascade comprises only Cas6f2, Cas5f2, and six Cas7f2 subunits, yet it retains full DNA targeting and degradation functionality. Our cryo-EM structure shows that Cas5f alone mediates PAM recognition via an AH domain that undergoes a conformational rearrangement upon engagement with the GG–PAM motif. This shift inserts a wedge helix into the major groove of the dsDNA, initiating strand separation and facilitating R-loop formation. This contrasts with Type I-E systems, where a glutamine wedge from the Cas8 large subunit inserts from the minor groove to initiate duplex melt-

ing. Thus, the I-F2 system adopts a more compact yet efficient mechanism for initiating interference.

Following PAM recognition and R-loop formation, the NTS is guided along a groove formed by the Cas7f backbone and directly handed off to Cas3. Unlike in I-E and I-F1 systems, where Cas3 is recruited in a helicase inactive or partially active state and activated upon docking, the Type I-F2 Cas3 is loaded in an active helicase conformation. Our structure shows that Cas3 is stably positioned via multivalent interactions with the central Cas7f subunits and Cas5f, forming a continuous path for NTS threading through the helicase domains. Notably, the CTD of Cas3, unresolved in previous Type I structures, adopts a defined conformation that may contribute to DNA coordination and stabilization of the complex. This architecture stabilizes the NTS trajectory and uniquely positions Cas3 for the immediate initiation of processive DNA degradation upon recruitment.

HDX-MS analysis supports this structural model by revealing protection patterns within the Cascade core upon DNA loading and R-loop formation, and Cas3 effector loading-associated changes likely linked to its activity state. These results underscore the functional sufficiency of a highly compact Cascade system in achieving precise and regulated interference.

Comparison to other type I mechanisms and evolutionary considerations

The mechanism observed in Type I-F2 represents a third mode of Cas3 recruitment among Type I systems: in contrast to Cas8-dependent allosteric activation in I-E and the constitutive loading seen in I-A, I-F2 relies on direct docking of an active Cas3 via a simplified, Cas8-independent architecture (Supplementary Fig. S10). This suggests that the core functional requirements of CRISPR interference, PAM sensing, R-loop formation, and Cas3 loading, can be implemented through markedly different structural solutions. Consistent with our EoT assays, Cas3 primarily evaluates the structural trajectory of the NTS rather than sequence identity at PAM-distal positions, explaining why some double mismatches are tolerated despite pronounced effects of single mismatches. Recent high-resolution structures of Type I-B and I-C Cascades [15] further expand this diversity, revealing additional variations in PAM sensing and effector engagement. Together with our Type I-F2 structure, these comparisons highlight the remarkable mechanistic plasticity of Cascade assemblies across the Type I family. Notably, the central positioning of Cas3 within the Type I-F2 Cascade shows mechanistic parallels to effector recruitment in Type IV-A systems, where the DinG helicase is docked directly onto the interference complex [69, 70]. Although Type IV-A complexes contain a Cas8-like subunit (Csf1), recent structures reveal that DinG is recruited to the core of the Type IV-A complex through extensive interactions with the Cas7-backbone subunits rather than being regulated via long-range allosteric activation. In this respect, both systems position their helicase effector centrally within the surveillance complex to enable direct engagement with the NTS, despite differences in overall subunit composition and evolutionary origin.

The minimization observed in Type I-F2 may reflect evolutionary pressures such as compatibility with MGEs, genome streamlining, or potential evasion of Acr mechanisms. Indeed, many characterized Acr proteins target the large subunit Cas8 or interfere with Cas3 recruitment interfaces in Type I-E and I-F1 systems. The complete absence of Cas8 in Type I-F2, together with pronounced structural divergence in Cas5f2 and Cas7f2, is therefore consistent with a possible evolutionary response to Acr-mediated inhibition. However, it should be emphasized that this interpretation remains speculative, as no Acr proteins targeting Type I-F2 systems have yet been identified or experimentally tested. Thus, while architectural simplification may contribute to functional robustness or avoidance of known Acr strategies, direct experimental evidence will be required to establish a causal link.

Implications and perspectives

This work provides a mechanistic and structural framework for understanding DNA interference by the most compact Type I CRISPR system known to date. By revealing how Cascade-mediated targeting and Cas3 engagement are achieved in the absence of a large subunit, our study expands the catalogue of known CRISPR interference mechanisms and highlights the evolutionary plasticity of Class 1 systems. The minimal size and simplified recruitment strategy of the I-F2 system make it an attractive candidate for genome engineering applications, especially in contexts where delivery vector capacity or system modularity is a limiting factor. Unlike Class 2 systems (Cas9/Cas12), which generate precise double-strand breaks [71, 72], the I-F2 Cas3 effector enables long-range DNA degradation [73], broadening the scope of CRISPR-based editing [74]. However, systematic evaluations of delivery efficiency, specificity, and performance in eukaryotic cells are still limited, and will be required to define the practical advantages and constraints of I-F2-based tools relative to established genome-editing platforms.

Together, these findings establish Type I-F2 as the most minimal yet fully competent Class 1 interference system, underscoring the versatility and evolutionary adaptability of CRISPR–Cas immunity.

Limitations

While the DNA substrate used in this study was engineered to stabilize a fully formed R-loop and therefore does not capture early surveillance or partial R-loop intermediates, this strategy allowed us to structurally resolve the interference-competent Type I-F2 effector complex. In Type I CRISPR–Cas systems, Cas3 engagement with Cascade is normally coupled to rapid DNA unwinding and degradation, which makes intact effector assemblies inherently transient. To enable structural analysis, two independent stabilization strategies are therefore required: first, engineering the DNA substrate to favor formation of a stable, fully formed R-loop; and second, preventing Cas3 turnover by omitting catalytic cofactors. Variants of these approaches have been widely used in structural studies of Type I CRISPR–Cas systems to capture interference-competent states that would otherwise be short-lived. Although this design limits direct insight into the earliest steps of duplex unwinding, extensive biochemical and structural evidence indicates that PAM-dependent DNA melting followed by stepwise crRNA:TS hybridization is conserved across Type I systems, as summarized in recent reviews [75]. Accordingly, we expect that similar principles govern DNA unwinding in Type I-F2 despite the absence of Cas8. The struc-

ture presented here thus represents a late-stage, interference-ready state rather than the full sequence of conformational transitions leading to R-loop formation. Functionally, the EoT assay provides a robust *in vivo* readout of interference efficiency but reports qualitative outcomes rather than kinetic parameters such as Cas3 loading rates or DNA degradation processivity. In addition, due to the repetitive architecture of the Cas7-backbone, HDX-MS cannot resolve dynamics at the level of individual Cas7 subunits or specific side-chain interfaces but instead reports on collective conformational stabilization associated with R-loop formation and Cas3 engagement. Nevertheless, the strong agreement between our cryo-EM structure, HDX-MS-derived conformational dynamics, and functional EoT assays supports the biological relevance of this stabilized complex and provides a mechanistic framework for Cas3 engagement and NTS processing in the minimal Type I-F2 system.

Acknowledgements

We thank the cryo-EM facility of the Institut Européen de Chimie et Biologie (Pessac, France) for the data collection time on the Talos Arctica microscope.

Author contributions: G.B., C.A.I., and P.P. designed the study. C.N.M and T.N.P. prepared the complex for cryo-EM. W.S. performed HDX-MS experiments. The EoT experiments were conducted by M.S.-L. T.N.P. prepared grids and performed cryo-EM data collection. T.N.P. and C.A.I. processed the cryo-EM data and built the model. T.N.P., C.N.M., L.R., C.A.I., P.P., and G.B wrote and revised the paper.

Supplementary data

Supplementary data is available at NAR online.

Conflict of interest

None declared.

Funding

G.B. has received funding from the Deutsche Forschungsgemeinschaft, DFG, (project nos 260989694, 324652314, and 405858511). C.A.I. is an EMBO YIP (project no. 3869) and has received funding from Inserm. P.P. receives funding from the Research Council of Lithuania, under the EMBO Installation Grant programme, under grant 5342-2023. Funding to pay the Open Access publication charges for this article was provided by Marburg University.

Data availability

The cryo-EM volume of the Type I-F2 Cascade–Cas3 effector complex has been deposited in the Electron Microscopy Data Bank under ID codes EMD 51023. The model for the Type I-F2 Cascade–Cas3 effector complex has been deposited in the PDB under ID code PDB 9G44. The HDX-MS data have been deposited to the ProteomeXchange Consortium via the PRIDE [62] partner repository with the dataset identifier PXD068253 and in short form as Supplementary Dataset S1. Raw cryo-EM data are available on request.

References

1. Barrangou R, Fremaux C, Deveau H *et al.* CRISPR provides acquired resistance against viruses in prokaryotes. *Science* 2007;315:1709–12. https://doi.org/10.1126/science.1138140
2. Brouns SJJ, Jore MM, Lundgren M *et al.* Small CRISPR RNAs guide antiviral defense in prokaryotes. *Science* 2008;321:960–4. https://doi.org/10.1126/science.1159689
3. Pourcel C, Salvignol G, Vergnaud G. CRISPR elements in *Yersinia pestis* acquire new repeats by preferential uptake of bacteriophage DNA, and provide additional tools for evolutionary studies. *Microbiology* 2005;151:653–63. https://doi.org/10.1099/mic.0.27437-0
4. Wang Y, Huang C, Zhao W. Recent advances of the biological and biomedical applications of CRISPR/Cas systems. *Mol Biol Rep* 2022;49:7087–100. https://doi.org/10.1007/s11033-022-07519-6
5. Nussenzweig PM, Marraffini LA. Molecular mechanisms of CRISPR–Cas immunity in bacteria. *Annu Rev Genet* 2020;54:93–120. https://doi.org/10.1146/annurev-genet-022120-112523
6. Gleditzsch D, Pausch P, Müller-Esparza H *et al.* PAM identification by CRISPR–Cas effector complexes: diversified mechanisms and structures. *RNA Biol* 2018;16:504–17. https://doi.org/10.1080/15476286.2018.1504546
7. Horvath P, Romero DA, Coûté-Monvoisin A-C *et al.* Diversity, activity, and evolution of CRISPR loci in *Streptococcus thermophilus*. *J Bacteriol* 2008;190:1401–12. https://doi.org/10.1128/JB.01415-07
8. Westra ER, van Erp PBG, Künne T *et al.* CRISPR immunity relies on the consecutive binding and degradation of negatively supercoiled invader DNA by Cascade and Cas3. *Mol Cell* 2012;46:595–605. https://doi.org/10.1016/j.molcel.2012.03.018
9. Makarova KS, Shmakov SA, Wolf YI *et al.* An updated evolutionary classification of CRISPR–Cas systems including rare variants. *Nat Microbiol* 2025;10:3346–61. https://doi.org/10.1038/s41564-025-02180-8
10. Makarova KS, Wolf YI, Koonin EV. Classification and nomenclature of CRISPR–Cas systems: where from here? *CRISPR J* 2018;1:325–36. https://doi.org/10.1089/crispr.2018.0033
11. Makarova KS, Wolf YI, Iranzo J *et al.* Evolutionary classification of CRISPR–Cas systems: a burst of class 2 and derived variants. *Nat Rev Micro* 2020;18:67–83. https://doi.org/10.1038/s41579-019-0299-x
12. Adler BA, Trinidad MI, Bellieny-Rabelo D *et al.* CasPEDIA Database: a functional classification system for class 2 CRISPR–Cas enzymes. *Nucleic Acids Res* 2024;52:D590–6. https://doi.org/10.1093/nar/gkad890
13. Shangguan Q, Graham S, Sundaramoorthy R *et al.* Structure and mechanism of the type I-G CRISPR effector. *Nucleic Acids Res* 2022;50:11214–28. https://doi.org/10.1093/nar/gkac925
14. Hu C, Ni D, Nam KH *et al.* Allosteric control of type I-A CRISPR–Cas3 complexes and establishment as effective nucleic acid detection and human genome editing tools. *Mol Cell* 2022;82:2754–68. https://doi.org/10.1016/j.molcel.2022.06.007
15. Lu M, Yu C, Zhang Y *et al.* Structure and genome editing of type I-B CRISPR–Cas. *Nat Commun* 2024;15:4126. https://doi.org/10.1038/s41467-024-48598-2
16. O'Brien RE, Santos IC, Wrapp D *et al.* Structural basis for assembly of non-canonical small subunits into type I-C Cascade. *Nat Commun* 2020;11:5931.
17. O'Brien RE, Bravo JPK, Ramos D *et al.* Structural snapshots of R-loop formation by a Type I-C CRISPR Cascade. *Mol Cell* 2023;83:746–58.
18. Hu C, Myers MT, Zhou X *et al.* Exploiting activation and inactivation mechanisms in Type I-C CRISPR–Cas3 for genome-editing applications. *Mol Cell* 2024;84:463–75. https://doi.org/10.1016/j.molcel.2023.12.034
19. McBride TM, Schwartz EA, Kumar A *et al.* Diverse CRISPR–Cas complexes require independent translation of small and large

subunits from a single gene. *Mol Cell* 2020;80:971–9. https://doi.org/10.1016/j.molcel.2020.11.003
20. Schwartz EA, McBride TM, Bravo JPK *et al.* Structural rearrangements allow nucleic acid discrimination by type I-D Cascade. *Nat Commun* 2022;13:2829. https://doi.org/10.1038/s41467-022-30402-8
21. Zhao H, Sheng G, Wang J *et al.* Crystal structure of the RNA-guided immune surveillance Cascade complex in *Escherichia coli*. *Nature* 2014;515:147–50. https://doi.org/10.1038/nature13733
22. Xiao Y, Luo M, Dolan AE *et al.* Structure basis for RNA-guided DNA degradation by Cascade and Cas3. *Science* 2018;361:eaat0839. https://doi.org/10.1126/science.aat0839
23. Guo TW, Bartesaghi A, Yang H *et al.* Cryo-EM structures reveal mechanism and inhibition of DNA targeting by a CRISPR–Cas surveillance complex. *Cell* 2017;171:414–26. https://doi.org/10.1016/j.cell.2017.09.006
24. Pausch P, Müller-Esparza H, Gleditzsch D *et al.* Structural variation of Type I-F CRISPR RNA guided DNA surveillance. *Mol Cell* 2017;67:622–32. https://doi.org/10.1016/j.molcel.2017.06.036
25. Rollins MF, Chowdhury S, Carter J *et al.* Structure reveals a mechanism of CRISPR-RNA-guided nuclease recruitment and anti-CRISPR viral mimicry. *Mol Cell* 2019;74:132–42. https://doi.org/10.1016/j.molcel.2019.02.001
26. Kim DY, Lee SY, Ha HJ *et al.* AcrIE7 inhibits the CRISPR–Cas system by directly binding to the R-loop single-stranded DNA. *Proc Natl Acad Sci USA* 2025;122:e2423205122. https://doi.org/10.1073/pnas.2423205122
27. Alalmaie A, Diaf S, Khashan R. Insight into the molecular mechanism of the transposon-encoded type I-F CRISPR–Cas system. *J Genetic Engineering Biotechnol* 2023;21:60. https://doi.org/10.1186/s43141-023-00507-8
28. Osakabe K, Wada N, Murakami E *et al.* Genome editing in mammalian cells using the CRISPR type I-D nuclease. *Nucleic Acids Res* 2021;49:6347–63. https://doi.org/10.1093/nar/gkab348
29. Kim DY, Lee SY, Ha HJ *et al.* Structural basis of Cas3 activation in type I-C CRISPR–Cas system. *Nucleic Acids Res* 2024;52:10563–74. https://doi.org/10.1093/nar/gkae723
30. Zhang M, Peng R, Peng Q *et al.* Mechanistic insights into DNA binding and cleavage by a compact type I-F CRISPR–Cas system in bacteriophage. *Proc Natl Acad Sci USA* 2023;120:e2215098120. https://doi.org/10.1073/pnas.2215098120
31. Liu Y, Wang L, Zhang Q *et al.* Structural basis for RNA-guided DNA degradation by Cas5-HNH/Cascade complex. *Nat Commun* 2025;16:1335. https://doi.org/10.1038/s41467-024-55716-7
32. Li X, Liu Y, Han J *et al.* Structural basis for the type I-F Cas8-HNH system. *EMBO J* 2024;43:4656–67. https://doi.org/10.1038/s44318-024-00229-8
33. Yadav G, Singh R. *In silico* analysis reveals the co-existence of CRISPR–Cas type I-F1 and type I-F2 systems and its association with restricted phage invasion in *Acinetobacter baumannii*. *Front Microbiol* 2022;13:909886. https://doi.org/10.3389/fmicb.2022.909886
34. Haurwitz RE, Jinek M, Wiedenheft B *et al.* Sequence- and structure-specific RNA processing by a CRISPR endonuclease. *Science* 2010;329:1355–8. https://doi.org/10.1126/science.1192272
35. Nuñez JK, Lee ASY, Engelman A *et al.* Integrase-mediated spacer acquisition during CRISPR–Cas adaptive immunity. *Nature* 2015;519:193–8.
36. Richter C, Gristwood T, Clulow JS *et al.* *In vivo* protein interactions and complex formation in the *Pectobacterium atrosepticum* subtype I-F CRISPR/Cas system. *PLoS One* 2012;7:e49549. https://doi.org/10.1371/journal.pone.0049549
37. Chowdhury S, Carter J, Rollins MF *et al.* Structure reveals mechanisms of viral suppressors that intercept a CRISPR RNA-guided surveillance complex. *Cell* 2017;169:47–57. https://doi.org/10.1016/j.cell.2017.03.012
38. Hayes RP, Xiao Y, Ding F *et al.* Structural basis for promiscuous PAM recognition in type I–E Cascade from *E. coli*. *Nature* 2016;530:499–503. https://doi.org/10.1038/nature16995
39. Yin P, Zhang Y, Yang L *et al.* Non-canonical inhibition strategies and structural basis of anti-CRISPR proteins targeting type I CRISPR–Cas systems. *J Mol Biol* 2023;435:167996. https://doi.org/10.1016/j.jmb.2023.167996
40. Bondy-Denomy J, Garcia B, Strum S *et al.* Multiple mechanisms for CRISPR–Cas inhibition by anti-CRISPR proteins. *Nature* 2015;526:136–9. https://doi.org/10.1038/nature15254
41. Xiao Y, Luo M, Hayes RP *et al.* Structure basis for directional R-loop formation and substrate handover mechanisms in Type I CRISPR–Cas system. *Cell* 2017;170:48–60. https://doi.org/10.1016/j.cell.2017.06.012
42. Dwarakanath S, Brenzinger S, Gleditzsch D *et al.* Interference activity of a minimal Type I CRISPR–Cas system from *Shewanella putrefaciens*. *Nucleic Acids Res* 2015;43:8913–23. https://doi.org/10.1093/nar/gkv882
43. Gleditzsch D, Müller-Esparza H, Pausch P *et al.* Modulating the Cascade architecture of a minimal Type I-F CRISPR–Cas system. *Nucleic Acids Res* 2016;44:5872–82. https://doi.org/10.1093/nar/gkw469
44. Makarova KS, Wolf YI, Alkhnbashi OS *et al.* An updated evolutionary classification of CRISPR–Cas systems. *Nat Rev Micro* 2015;13:722–36. https://doi.org/10.1038/nrmicro3569
45. Carpenter MR, Kalburge SS, Borowski JD *et al.* CRISPR–Cas and contact-dependent secretion systems present on excisable pathogenicity islands with conserved recombination modules. *J Bacteriol* 2017;199:e00842–16. https://doi.org/10.1128/JB.00842-16
46. Labbate M, Orata FD, Petty NK *et al.* A genomic island *in vibrio* cholerae with VPI-1 site-specific recombination characteristics contains CRISPR–Cas and type VI secretion modules. *Sci Rep* 2016;6:36891. https://doi.org/10.1038/srep36891
47. Ma S, Zhang S, Liu K *et al.* Efficient, compact, and versatile: type I-F2 CRISPR–Cas system. *mLife* 2024;3:384–6. https://doi.org/10.1002/mlf2.12145
48. Guo J, Gong L, Yu H *et al.* Engineered minimal type I CRISPR–Cas system for transcriptional activation and base editing in human cells. *Nat Commun* 2024;15:7277. https://doi.org/10.1038/s41467-024-51695-x
49. Chen Y, Liu J, Zhi S *et al.* Repurposing type I–F CRISPR–Cas system as a transcriptional activation tool in human cells. *Nat Commun* 2020;11:3136. https://doi.org/10.1038/s41467-020-16880-8
50. Mastronarde DN. Automated electron microscope tomography using robust prediction of specimen movements. *J Struct Biol* 2005;152:36–51. https://doi.org/10.1016/j.jsb.2005.07.007
51. Kimanius D, Dong L, Sharov G *et al.* New tools for automated cryo-EM single-particle analysis in RELION-4.0. *Biochem J* 2021;478:4169–85. https://doi.org/10.1042/BCJ20210708
52. Zheng SQ, Palovcak E, Armache J-P *et al.* MotionCor2: anisotropic correction of beam-induced motion for improved cryo-electron microscopy. *Nat Methods* 2017;14:331–2. https://doi.org/10.1038/nmeth.4193
53. Rohou A, Grigorieff N. CTFFIND4: fast and accurate defocus estimation from electron micrographs. *J Struct Biol* 2015;192:216–21. https://doi.org/10.1016/j.jsb.2015.08.008
54. Afonine PV, Poon BK, Read RJ *et al.* Real-space refinement in PHENIX for cryo-EM and crystallography. *Acta Crystallogr D Struct Biol* 2018;74:531–44. https://doi.org/10.1107/S2059798318006551
55. Pettersen EF, Goddard TD, Huang CC *et al.* UCSF Chimera—a visualization system for exploratory research and analysis. *J Comput Chem* 2004;25:1605–12. https://doi.org/10.1002/jcc.20084
56. Terwilliger TC, Sobolev OV, Afonine PV *et al.* Automated map sharpening by maximization of detail and connectivity. *Acta Crystallogr D Struct Biol* 2018;74:545–59. https://doi.org/10.1107/S2059798318004655

57. Emsley P, Cowtan K. Coot: model-building tools for molecular graphics. *Acta Crystallogr D Biol Crystallogr* 2004;60:2126–32. https://doi.org/10.1107/S0907444904019158
58. Croll TI. ISOLDE: a physically realistic environment for model building into low-resolution electron-density maps. *Acta Crystallogr D Struct Biol* 2018;74:519–30. https://doi.org/10.1107/S2059798318002425
59. Adams PD, Afonine PV, Bunkóczi G *et al.* PHENIX: a comprehensive Python-based system for macromolecular structure solution. *Acta Crystallogr D Biol Crystallogr* 2010;66:213–21. https://doi.org/10.1107/S0907444909052925
60. Osorio-Valeriano M, Altegoer F, Steinchen W *et al.* ParB-type DNA segregation proteins are CTP-dependent molecular switches. *Cell* 2019;179:1512–24.e15. https://doi.org/10.1016/j.cell.2019.11.015
61. Wales TE, Fadgen KE, Gerhardt GC *et al.* High-speed and high-resolution UPLC separation at zero degrees Celsius. *Anal Chem* 2008;80:6815–20. https://doi.org/10.1021/ac8008862
62. Perez-Riverol Y, Bandla C, Kundu DJ *et al.* The PRIDE database at 20 years: 2025 update. *Nucleic Acids Res* 2025;53:D543–53. https://doi.org/10.1093/nar/gkae1011
63. Rollins MF, Chowdhury S, Carter J *et al.* Cas1 and the Csy complex are opposing regulators of Cas2/3 nuclease activity. *Proc Natl Acad Sci USA* 2017;114:E5113–21. https://doi.org/10.1073/pnas.1616395114
64. Van der Oost J, Westra ER, Jackson RN *et al.* Unravelling the structural and mechanistic basis of CRISPR–Cas systems. *Nat Rev Micro* 2014;12:479–92. https://doi.org/10.1038/nrmicro3279
65. Van Erp PBG, Patterson A, Kant R *et al.* Conformational dynamics of DNA binding and Cas3 recruitment by the CRISPR RNA-guide cascade complex. *ACS Chem Biol* 2018;13:481–90. https://doi.org/10.1021/acschembio.7b00649
66. Klein N, Sanchez-Londono M, Kara MM *et al.* Type I-Fv and engineered type IV-A1 CRISPR–Cas effectors facilitate genome reduction in *Escherichia coli*. *Nucleic Acids Res* 2025;53:gkaf1399. https://doi.org/10.1093/nar/gkaf1399
67. Hu C, Ke A. Reconstitution and biochemical characterization of the RNA-guided helicase-nuclease protein Cas3 from type I-A CRISPR–Cas system. *Methods Enzymol* 2022;673:405–24.
68. Huo Y, Nam KH, Ding F *et al.* Structures of CRISPR Cas3 offer mechanistic insights into Cascade-activated DNA unwinding and degradation. *Nat Struct Mol Biol* 2014;21:771–7. https://doi.org/10.1038/nsmb.2875
69. Cui N, Zhang J-T, Liu Y *et al.* Type IV-A CRISPR-Csf complex: assembly, dsDNA targeting, and CasDinG recruitment. *Mol Cell* 2023;83:2493–508. https://doi.org/10.1016/j.molcel.2023.05.036
70. Čepaitė R, Klein N, Mikšys A *et al.* Structural variation of types IV-A1- and IV-A3-mediated CRISPR interference. *Nat Commun* 2024;15:9306.
71. Zetsche B, Gootenberg JS, Abudayyeh OO *et al.* Cpf1 is a single RNA-guided endonuclease of a class 2 CRISPR–Cas system. *Cell* 2015;163:759–71. https://doi.org/10.1016/j.cell.2015.09.038
72. Jinek M, Chylinski K, Fonfara I *et al.* A programmable dual-RNA-guided DNA endonuclease in adaptive bacterial immunity. *Science* 2012;337:816–21. https://doi.org/10.1126/science.1225829
73. Morisaka H, Yoshimi K, Okuzaki Y *et al.* CRISPR–Cas3 induces broad and unidirectional genome editing in human cells. *Nat Commun* 2019;10:5302. https://doi.org/10.1038/s41467-019-13226-x
74. Sanchez-Londono M, Rust S, Hernández-Tamayo R *et al.* Visualization of Type IV-A1 CRISPR-mediated repression of gene expression and plasmid replication. *Nucleic Acids Res* 2024;52:12592–603. https://doi.org/10.1093/nar/gkae879
75. Liu TY, Doudna JA. Chemistry of Class 1 CRISPR–Cas effectors: binding, editing, and regulation. *J Biol Chem* 2020;295:14473–87. https://doi.org/10.1074/jbc.REV120.007034

Received: November 13, 2025. **Revised:** January 28, 2026. **Accepted:** February 2, 2026